

Project Report

Understanding Intracuster-medium of Coma Cluster

By

Chandraniva Guha Ray and Aditi Sinha,

Indian Institute of Science Education and Research, Kolkata



Under the supervision of

Dr. Yvette Perrott and Dr. Tulasi Parashar ,

Victoria University of Wellington, New Zealand



February, 2021 -

ABSTRACT

Aim of this research project is to understand the turbulence in Intracluster medium of Coma Galaxy Cluster by analyzing the pressure perturbations in it using Sunyaev-Zeldovich effects. In order to understand the turbulence, MILCA Map was used to compute both the power spectrum and the cross power spectra of normalised y fluctuations. Here, the SZ y map is bin averaged over the Cluster radius in bins of 3 arcmin to get a y profile. The y profile has been deprojected using an "onion peeling" method to get the corresponding pressure profile. Both the y profile and deprojected pressure profile is fit with the beta model to estimate the pressure power spectrum from the y power spectrum. However, the pressure power spectrum is observed to be a strong function of the physical distance from the centre. The y fluctuations were further tested on an elliptical model of the galaxy cluster. The report gives a detailed explanation of the techniques adopted in order to do so. The code made throughout this project is available at: **[Github ICM project](#)**

1 CHAPTER 1

INTRODUCTION

Galaxy Clusters are large massive objects in the universe which consists of hundreds to thousands of galaxies bound together by Gravity. One of the key features of these objects is the Intracuster-medium (ICM). This heated gas between the galaxies inside the cluster is an important research topic in the current world. We are using European Space Agency's Planck mission data to get the thermal sunyaev-zeldovich fluctuations.

Studies of the cosmic microwave background radiation revolve about how its interactions with clusters of galaxies provide an astrophysical and cosmological probe. The thermal Sunyaev-Zel'dovich effect measures the strength of interaction between hot gas in a cluster and the cosmic microwave background.

1.1 SUNYAEV-ZELDOVICH EFFECT

1.1.1 Compton Scattering

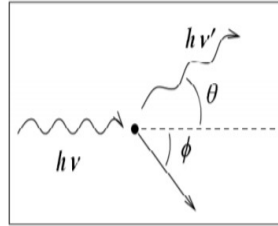


Figure 1: Compton Scattering

When an energetic photon interacts with a charged particle such as an electron, it gives it an impulse transferring momentum, losing energy in the process. This is known as the Compton scattering.

If ν and ν' are the frequencies of the photon before and after the scattering, m_0 is the rest mass and E is the energy of the charged particle (Figure 1), then conservation of energy would imply,

$$m_0c^2 + h\nu = E + h\nu'$$

where, $E = M\gamma c^2$ and $\gamma = 1/\sqrt{(1 - v^2)/c^2}$ is the lorentz factor.
Conservation of momentum along the direction of the incident photon :

$$\frac{h\nu}{c} = \frac{h\nu' \cos \theta}{c} + m_0\gamma\nu \cos \phi$$

whereas momentum conservation in the transverse direction gives

$$0 = \frac{h\nu' \sin \theta}{c} + m_0\gamma\nu \sin \phi$$

These equations can be solved to give, in terms of the wavelengths

$$\lambda' - \lambda = 2\lambda_c \sin^2 \frac{\theta}{2}$$

where, $\lambda_c = h/m_0c$ is the compton wavelength of the particle.

1.1.2 Inverse Compton Scattering

One also encounters an opposite effect, of energetic particles transferring momentum to low energy photons, which is known as the inverse Compton scattering.

The two processes - compton and inverse compton scattering can be thought of as manifestations of the same process viewed in two different frames of reference. If the observer is at rest with respect to the energetic electron, the inverse Compton scattering would appear as the normal Compton scattering, since to the observer the photon would appear to be highly energetic and being scattered by a stationary particle.

Considering a case when the electron is not stationary and the photon collides with it at an angle α to the trajectory of the electron. If we view this process from electron's perspective, then we see the photon to be blue-shifted (i.e., displacement to shorter wavelength) to $h\nu' = \gamma h\nu(1 - v \cos(\alpha)/c)$. So, photons with $\alpha = 0$ appear to be at low energy relative to the electron, whereas the ones with $\alpha = \pi$ appear to be blue shifted to $h\nu' \approx \gamma h\nu$. Considering, the low energy limit (Thomson scattering) limit of Compton interaction, then in the frame of reference of the electron, we see no appreciable frequency shift. Hence the scattered photon has energy $h\nu'' \approx h\nu' \approx \gamma h\nu$.

When high energy photons interact with electrons, the exchange of energy between them can lead to distinct changes in the photon spectrum and the energy content of the electrons. Exchange of energy happens both ways - electron recoil results into energy transfer from photons to electrons and high velocities of electron tend to transfer their Kinetic Energy to photons.

One can express the degree of interaction between photons and electrons by a parameter y , where

$$y = k_B T_e m_e c^2 n_e \sigma_T L$$

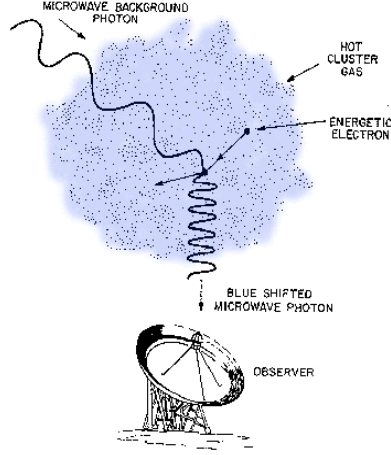


Figure 2: Schematic representation of Sunyaev Zeldovich Effect

where T_e is the temperature of the electrons, n_e is their number density and L is the size of the gaseous system.

The **Sunyaev-Zel'dovich effect**, thus, arises from the scattering of electrons in clusters of galaxies on the cosmic microwave background radiation. The effect provides a cosmological probe, which can be used to measure the properties of gas in clusters of galaxies.

2 CHAPTER 2

ANALYZING THE DATA

As the blackbody photons from the Cosmic Microwave Background interact with hot intracluster medium traveling from the last scattering surface to us, Compton scattering up-scatters a fraction of photons to higher energy creating a distortion from the Planck spectrum T_ν^{planck} . The change in the intensity, $\Delta I_\nu = I_\nu - I_\nu^{Planck}$ of the CMB radiation is given by

$$\Delta I_\nu = y \frac{2h\nu^3}{c^2} \frac{xe^x}{(e^x - 1)^2} \left[x \frac{(e^x + 1)}{(e^x - 1)} - 4 \right]$$

where, $x = h\nu/K_B T$, CMB temperature: $T = 2.725(1 + z)$ at redshift z , $\nu = \nu_0(1 + z)$ is the frequency of CMB photon at redshift z , ν_0 is the observed frequency at $z=0$, h is the planck's constant, k_B is the Boltzmann constant and c is the speed of light. "y" here is the amplitude of distortion. It is proportional to the integral of the pressure P along the line of sight,

$$y = \frac{\sigma_T}{m_e c^2} \int ds n_e k_B T_e$$

where, T_e and n_e are the electron temperature and electron number density respectively in the Intracluster Medium, m_e is the mass of the electron, σ_T is the Thompson scattering cross-section, and s is the distance coordinate along the line of sight. The Sunyaev-Zeldovich amplitude, y , contains information about the properties of the galaxy cluster which in turn are sensitive to the cosmological parameters. In this project, we are using y maps created using the data from Planck (ESA space probe) to study clusters. Particularly, we have used the MILCA y maps available publicly in the Planck website. The probe detects y signal upto a few Mega parsecs, which opens up the possibility of studying the perturbations in ICM on large scales. It is crucial to understand the physics of the ICM, as hot gaseous haloes have been found to be ubiquitous from massive galaxy clusters to elliptical and spiral galaxies, the cascading large-scale turbulence in the hot halo can also drastically alter the accretion mode onto the central super massive black hole, igniting 'chaotic cold accretion'. Being the largest collapsed structures, galaxy clusters are highly sensitive to the cosmological parameters. To achieve high-precision cosmology, however, we require precise estimates of the cluster masses, minimizing errors and scatter.

2.1 Choice of Cluster

For this study, we have chosen the Coma Cluster (Abell 1656) which is one of the biggest galaxy clusters near us. Coma is classified as a hot, massive galaxy cluster with average core plasma temperature 8.5 keV. The coma cluster is situated at a redshift of $z = 0.0232$. The cluster is a good cluster to study as it has the highest signal to noise ratio in Planck data and it is relatively situated in an uncontaminated region of the sky. Coma is an archetypal non-cool-core cluster with radiative cooling time greater than the Hubble time. The distance of cluster is taken to be 93 Mpc. At this distance $1 \text{ arcmin} = 27.05 \text{ kpc}$.

2.2 y Profile in Bins

The MILCA y map consists of 700×700 pixels covering a physical distance of $20^\circ \times 20^\circ$. Thus, 1 pixel corresponds to 1.718 arcmin. The map is shown in figure 3.

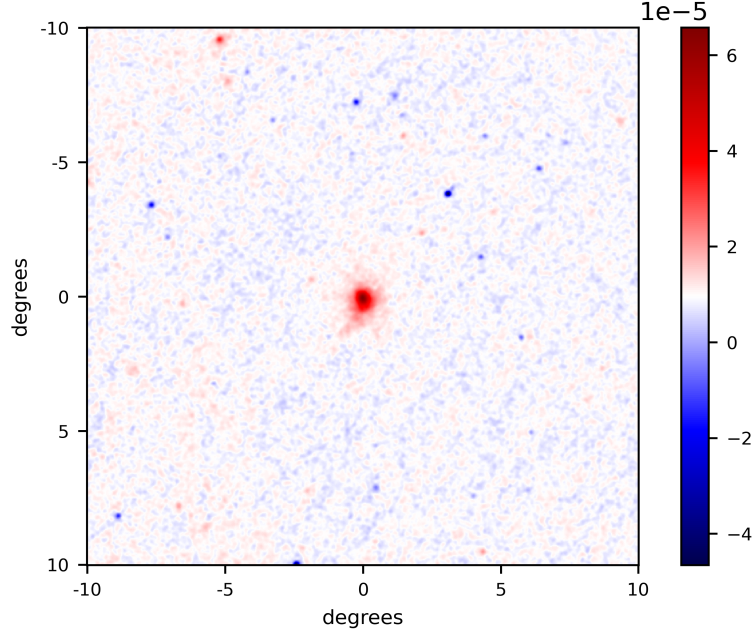


Figure 3: MILCA y map of Coma Cluster with centre of the map (NOT Cluster) at WCS coordinates (58.06, 87.96)

Before proceeding, we would like to know the location of the centre of the cluster but that is not as straightforward. In fact, the y fluctuation maps (covered in section 2.4) are highly sensitive to our choice of centre coordinates. The obvious choice of coordinate (350, 350) might not correspond the actual centre of the cluster. Choosing the coordinate corresponding to the highest y value may be one choice. But, we have chosen our optimal centre coordinates according to a different criteria involving the minimization of a dipole metric for y fluctuations map. The entire procedure has been described in section 2.5. The centre values we have used for the subsequent analysis corresponds to (352.42, 349.86) in terms of pixels.

To calculate the y profile, \bar{y} from the MILCA map of Coma cluster (Figure 4), we take the average of all pixels in bins (i.e., rings) of radius 3 arcmins or 81 kpc. Thus, the area swept by the bins increases as we move further away from the centre. The profile is then fit with a beta model for $\theta < 2000$ kpc (figure 4), where the β model is defined as

$$\bar{y}_\beta(\theta) = \frac{y_0}{(1 + \theta^2/\theta_c^2)^\beta}$$

The β -model is found to be a good fit to the y profile with for $\theta < 1200$ kpc but shows

deviation at larger distances as observed in the figure 4.

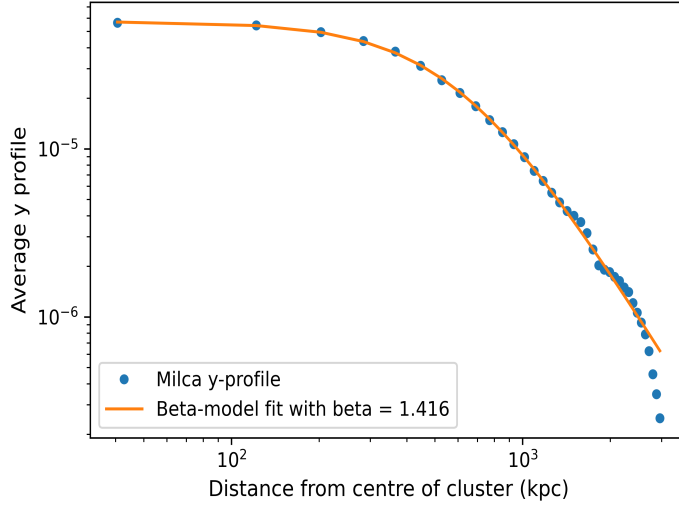


Figure 4: Average y profile, $\bar{y}(\theta)$ in bins of 3 arcmins fit with a beta model. The optimized beta model parameters were found out to be $y_0 = 5.71 \times 10^{-5}$, $\theta_c = 615.44 \text{ kpc}$ and $\beta = 1.416$

2.3 Deprojection using "onion peeling"

In order to get 3D pressure profile from the 2D y profile, we need to carry out a deprojection. Instead of doing an Abel transform for this (as described in Khatri and Gaspari, 2012), we take a more numerical approach. The equation relating the two is given by,

$$[y_{2D}] = [R_{PROJ}] [y_{3D}]$$

where $[y_{2D}]$ and $[y_{3D}]$ are column vectors of n dimensions, n being the total number of annuli. Note that the factor mc^2/T_e has not been taken into account here. These are as of yet, just bin averaged "3D y" values. We will be essentially constructing a $n \times n$ projection matrix whose $(i, j)^{th}$ element will represent the fraction of emission from annulus "j" that would be observed by a "perfect" detector to fall in annulus "i". Thus, the deprojected "3D y" values will be given by,

$$[y_{3D}] = [R_{PROJ}]^{-1} [y_{2D}]$$

The projection matrix is constructed using the following algorithm (See Figure 5):

$$n'_{cl}(R_{i-1}, R_i) = \frac{N_{cl}(R_{i-1}, R_i) - \sum_{j=i+1}^m [n_{cl}(R_{j-1}, R_j) V_{int}(R_{j-1}, R_j; R_{i-1}, R_i)]}{V_{int}(R_{i-1}, R_i; R_{i-1}, R_i)}$$

where,

$$V_{int}(r_{j-1}, r_j; R_{i-1}, R_i) = \frac{4\pi}{3} [(r_j^2 - R_i^2)^3/2 + (r_{j-1}^2 - R_i^2)^3/2 - (r_{j-1}^2 - R_{i-1}^2)^3/2]$$

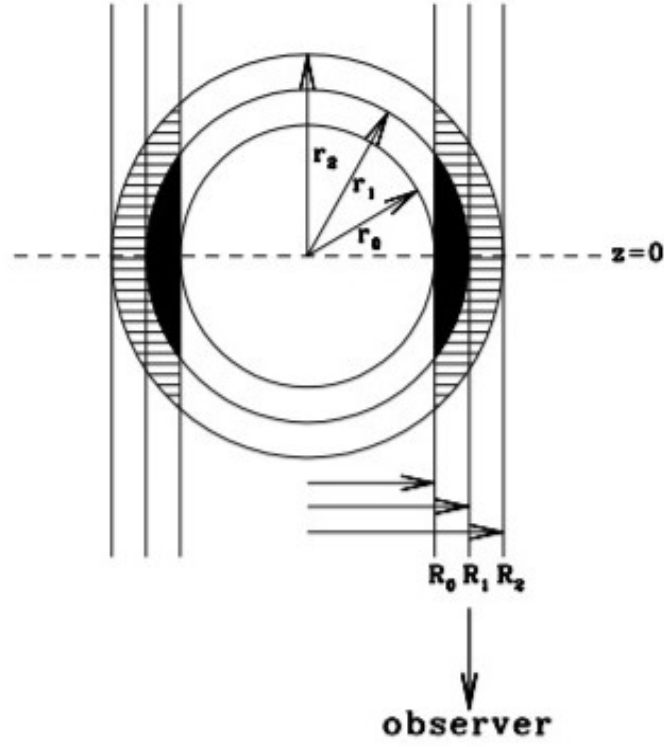


Figure 5: Geometrical deprojection Algorithm, Source: MacLaughlin, 1999

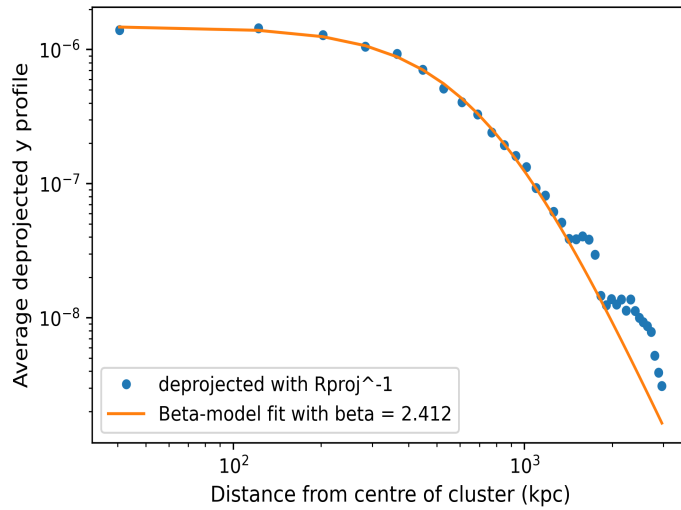


Figure 6: Deprojected y profile using "onion peeling". The optimized beta model parameters were found out to be $(y_0)_{3D} = 1.48 \times 10^{-6}$, $r_c = 745.15 \text{ kpc}$ and $\beta_{3D} = 2.412$

Thus,

$$n'_{cl}(R_{i-1}, R_i) = \frac{3}{4 \times (R_i^2 - R_{i-1}^2)^{1/2}} \times \left[N_{cl}(R_{i-1}, R_i) - \sum_{j=i+1}^m \frac{n_{cl}(R_{j-1}, R_j) V_{int}(R_{j-1}, R_j; R_{i-1}, R_i)}{\pi(R_i^2 - R_{i-1}^2)} \right]$$

For more details, see Croston et al. (2006) and Appendix A of MacLaughlin (1999). The deprojected y profile was also fit with a beta model with some slight changes,

$$\bar{y}_\beta(\theta) = \frac{(y_0)_{3D}}{(1 + r^2/r_c^2)^{\beta_{3D}}}$$

where r is the 3D distance from the centre, with $r^2 = \theta^2 + z^2$, z being the depth from the plane of observation. The final profile along with beta fit is shown in figure 6.

Note: Planck is not a "perfect" detector as it has a finite resolving power. The resolution of the instrument, known as the point spread function (PSF) hasn't been taken into account while deprojecting. The issue has been further discussed in the next section 2.4.

2.4 The issue of PSF

Planck has a finite resolving power of about 10 arcmins. This is much bigger than the resolution of Chandra and other X-ray devices. We need to take care of this while deprojecting since the received signal has already been convoluted with the PSF function which is a Gaussian with FWHM of about 10 arcmins. The new equation relating the 2D y and "3D y" thus becomes,

$$[y_{2D}] = [R_{PSF}] [R_{PROJ}] [y_{3D}]$$

where $[R_{PSF}]$ is another $n \times n$ matrix whose $(i, j)^{th}$ element represents the redistribution of counts from an annulus "j" of the ideal profile to annulus "i" of the actual profile resulting from the effect of the PSF. Thus, the deprojected "3D y" values taking into account the PSF becomes,

$$[y_{3D}] = [R_{PROJ}]^{-1} [R_{PSF}]^{-1} [y_{2D}]$$

We performed a small simulation to check the validity of both the projection and PSF matrices and observed that there was significant deviation of the retrieved signal from the original signal used (Figure 7). Upon further inspection, we discovered that the problem arises while taking the inverse of the PSF matrix (Figure 8). Some of the off-diagonal elements of $[R_{PSF}]$ take values that are very close to 0 which might be causing a numerical instability in the computation of its inverse. This particular issue was also mentioned in Croston et al. (2006) and the solution might involve using a more sophisticated Lagrange multipliers method. A more detailed study is required before the values of the beta model parameters for the deprojected y profile (Figure 6) can be trusted.

Note: These values have been used in section 4 while converting the y power spectrum to pressure power spectrum, specifically while computing the values of N's.

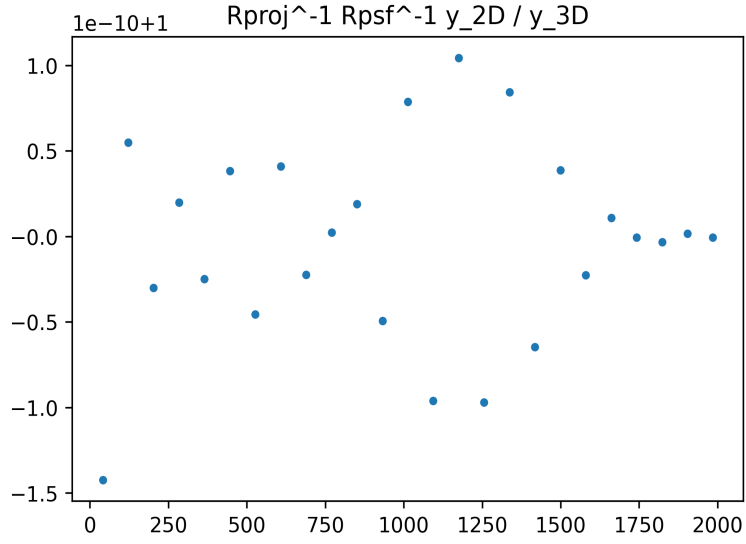


Figure 7: The ratio of retrieved y_{3D} to th original y_{3D} vs distance from the centre of the simulated cluster

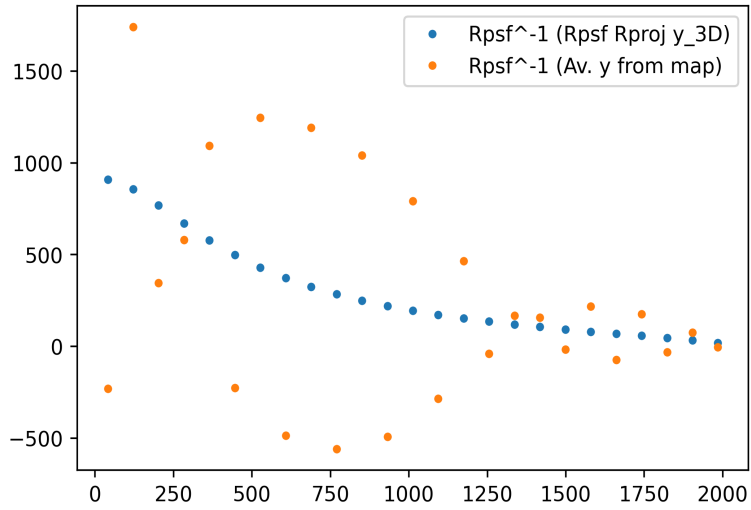


Figure 8: Testing the validity of $[R_{PSF}]^{-1}$. The figure clearly shows that the inverse of the matrix is unstable.

2.5 y fluctuations

Now, we calculate the SZ fluctuations (δy) for a $4^\circ \times 4^\circ$ region around the centre of the cluster by removing the average y profile, $\bar{y}(\theta)$. This is done by interpolating between the bin-averaged y profile values to estimate y at any distance from the center. For each pixel, this estimated average y value is subtracted to get the fluctuation map. So, δy is given by:

$$\delta y = y - \bar{y}$$

The fluctuation map is shown in figure 9. Note that such a process doesn't require us to assume any underlying model like the beta model making the δy map independent of the model parameters.

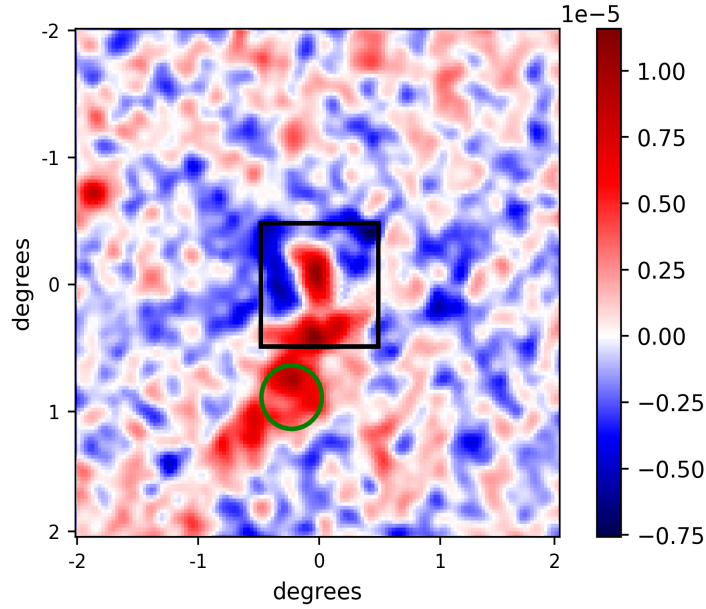


Figure 9: SZ fluctuations, δy map of Coma with the rectangular black patch indicating where centre optimization to reduce dipole was carried out and the green circular patch indicating the brightest galaxy of the cluster (NGC4839)

We also want to calculate the normalized fluctuation map by dividing with the average y profiles, i.e., $\frac{\delta y}{\bar{y}}$, because it is the relative perturbations that are of physical significance, not the absolute perturbations. The normalized fluctuation map is shown in figure 8. Another important thing to note about figure 8 is that the normalised fluctuations diverge to large values very quickly for physical distances $\theta > 1620$ kpc (1 degree). Thus, the values greater than 1.5 and less than -1.5 have been cutoff in figure 8 to better visualise the normalised fluctuations around the centre.

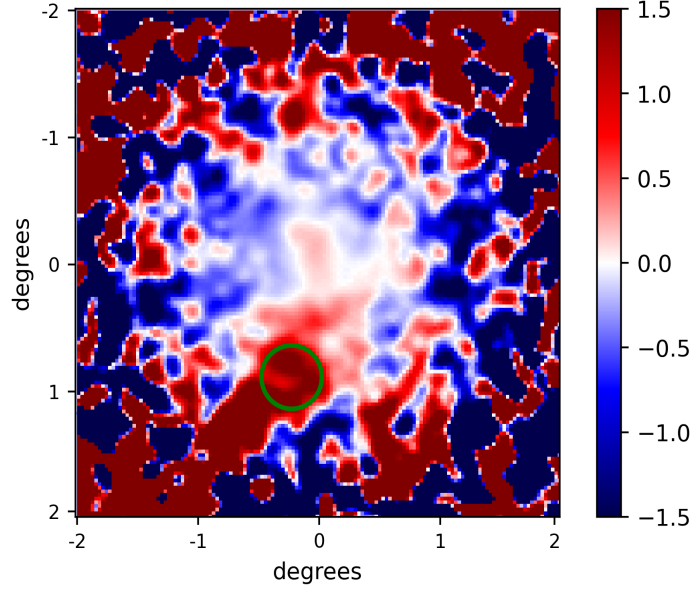


Figure 10: Normalized SZ fluctuations, $\frac{\delta y}{y}$ in Coma cluster with the green circular patch indicating the brightest galaxy of the cluster (NGC4839)

2.6 Optimization of centre and elliptical model

Now that we have a pipeline ready for the fluctuation map of a given y map, we can try to optimize the centre coordinates and even try to fit an elliptical model for the cluster. **Optimization of the parameters is crucial because the fluctuation map is very sensitive to changes in centre coordinates and the elliptical model parameters.** The elliptical model is given by,

$$r^2(x, y) = \left[f \cos^2 \theta + \frac{\sin^2 \theta}{f} \right] x^2 + \left[f \sin^2 \theta + \frac{\cos^2 \theta}{f} \right] y^2 + 2 \cos \theta \sin \theta \left[f - \frac{1}{f} \right] xy$$

where (x, y) is the distance from the centre, f is the minor-to-major axis ratio and θ is the angle between the major axis and the north direction.

The metric we have chosen to carry out this optimization is given by the absolute sum of pixels around the centre. The area around the centre chosen to decide whether a pixel contributes to sum or not is depicted in figure 7 by the black rectangular patch. Such a metric was chosen because we observed a strong dipole structure near the centre, which we are essentially trying to minimize. The resulting behaviour of the metric in parameter space (x, y) is shown in figure 9.

Both the optimization of the centre coordinates and the elliptical model parameters are done simultaneously, first by scanning over all of the parameter space to get a rough estimate of

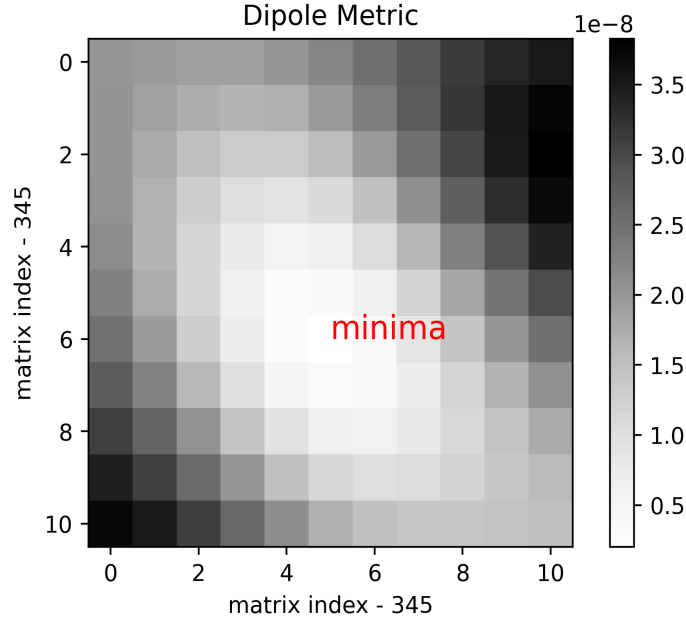


Figure 11: Metric behaviour around the centre. Both the x and y axes lies in the range of 345 to 355 pixels (since the original map was 700×700 pixels).

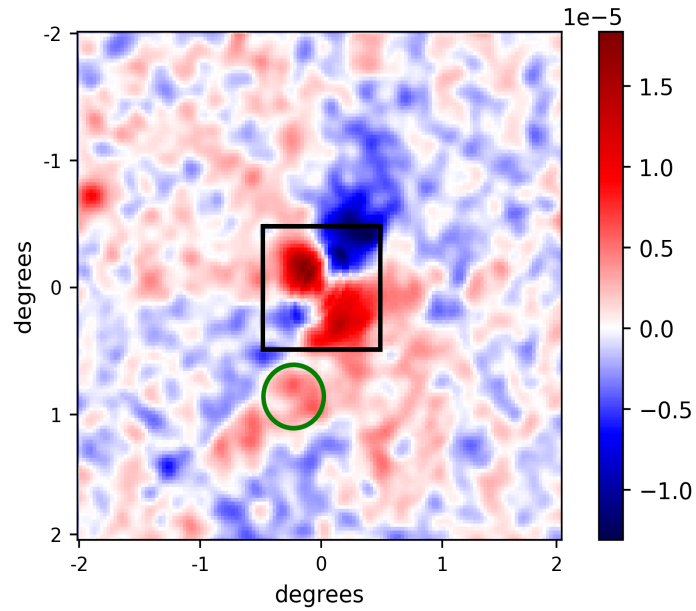


Figure 12: Skewed fluctuation map ($f=0.52$) with the rectangular black patch indicating where centre optimization to reduce dipole was carried out and the green circular patch indicating the brightest galaxy of the cluster (NGC4839)

the optimal values and then by performing a gradient descent for a finer result. The optimal parameters for the original map was found out to be $(x, y, f, \theta) = (352.42, 349.85, 0.89, -0.64)$. However, we are unsure about the incorporation of elliptical model in the calculation of power spectrum (section 3), so we stuck to a spherical model with $(x, y, f, \theta) = (352.42, 349.85, 1.00, 0)$

We also noted that the metric may not be a convex function in the parameter space (f, θ) and another local minima was obtained at $f=0.52$. The resulting fluctuation map is shown in figure 10. Coma may not be spherically symmetric but definitely doesn't happen to be that drastically skewed, and thus the metric needs further analysis.

With this, we proceed to calculate the power spectrum in the next section 3.

3 CHAPTER 3

POWER SPECTRUM CALCULATIONS

The galaxy correlation function is a measure of the degree of clustering in either the spatial ($\xi(r)$) or the angular distribution ($w(\theta)$) of galaxies. **The power spectrum is the Fourier transform of the correlation function.** The spatial two-point or auto correlation function is defined as the excess probability, compared with that expected for a random distribution, of finding a pair of galaxies at a separation r_{12} :

$$dP = \bar{n}^2(1 + \xi(r_{12}))dV_1dV_2$$

where \bar{n} is the mean galaxy density. On small scales, $0.1h^{-1}Mpc \leq r \leq 10h^{-1}Mpc$, the spatial correlation function is well described by a power law form $\xi(r) = (r_0/r)^\gamma$, with slope $\gamma \approx 1.8$ and a correlation length $r_0 \approx 5h^{-1}Mpc$. The angular galaxy correlation function can also be written as a power law, with $w(\theta) = A\theta^{(1-\gamma)}$, where 'A' depends upon the depth of the galaxy sample, due to dilution of the clustering signal as a result of projection effects. The power spectrum $P(k)$ is related to the two-point correlation function by:

$$\xi(r) = \frac{1}{2\pi^2} \int dk \cdot k^2 P(k) \frac{\sin kr}{kr}$$

The scale or wavelength λ of a fluctuation is related to the wavenumber, k by $k = 2\pi/\lambda$

Throughout the project, we have used the publicly available software **NaMaster** to compute the power spectrum of maps. The software computes the angular power spectrum in bins of l 's where l is the multipole given by

$$l = \frac{\pi}{\theta_{separation}}$$

where $\theta_{separation}$ is the angular separation related to the spatial distance by the conversion factors described before.

3.1 Flat Sky Approximation

We are also using the flat-sky approximation, as described in Appendix A of Khatri and Gaspari (2012) to convert the angular power spectrum C_l back to non angular power spectrum P_k for ease of analysis. The correlation function is written in terms of Fourier Space as well as in spherical harmonic space. Equating these two ways of calculating the same correlation function gives us the flat sky relation between the two power spectra. This essentially boils down to the relation,

$$l^2 C_l = k^2 P(k)$$

For the derivation of the relation, refer to Appendix A of Khatri and Gaspari, 2012.

3.2 Masking and Apodization

Masking and apodization of maps are essential to prevent the fourier transform to behave badly. The mask is a map consisting of 1's in the region occupied by Coma and 0s everywhere else which leaves 60 arcmin radius region at the position of the Coma cluster unmasked. We apodize the mask before multiplication with the y-map to avoid high-frequency artefacts in power spectrum due to the sharp edges in the mask. Although NaMaster provides its own apodization routines, we chose to follow the scheme described in (1). The apodization is done using a 15 arcmin Gaussian replacing the 1's in the mask by $1 - \exp(9\theta_{edge}^2/(2\theta_{ap}^2))$ with $\theta_{ap} = 15$ arcmin. Here $\theta_{edge} = 1^\circ - \theta_{centre}$, with θ_{centre} being the distance from the centre of the cluster. The apodized mask is shown in figure 11.

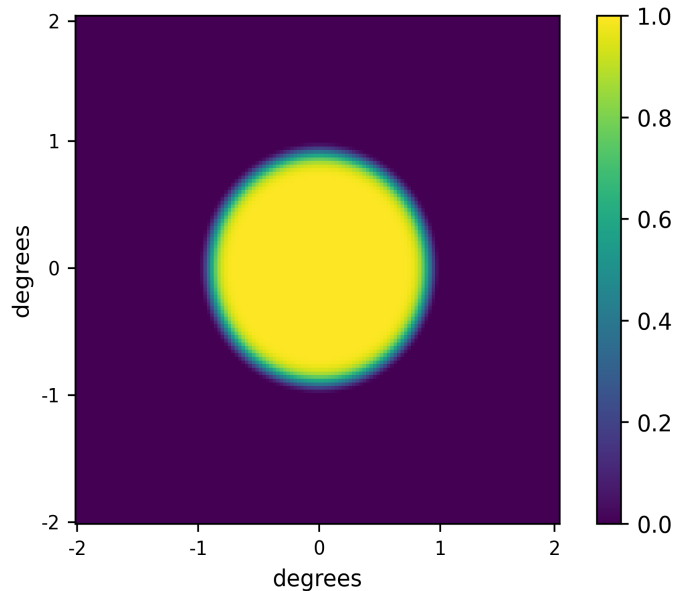


Figure 13: Apodized mask, using a gaussian smoothing with $\theta_{ap} = 15$ arcmin

3.3 Creating bins

NaMaster requires us to input bins in which power spectrum is to be calculated. For our purposes, we chose to create 6 bins between 500 kpc and 2000 kpc. These were converted in terms of l 's using the conversion factors and $l = \frac{\pi}{\theta_{separation}}$. The lower bound was chosen to be 500 kpc as it should ideally be more than the resolving power of our instrument. Since Planck's resolution power of 10 arcmin corresponds to around 270 kpc, we roughly choose the lower bound as twice that value (i.e, 500 kpc). The upperbound is chosen such that it corresponds to roughly the radius of the cluster (i.e, 2000 kpc). Thus, we will be roughly probing the pressure perturbations in this scale. The bin number was chosen to be small enough to minimize the correlation between the neighbouring bins, which are expected when we do not have full sky, and large enough so that there are enough bins that the shape of the power spectrum is not washed out.

3.4 Beam

Before we can start looking at the power spectrum, we need to carefully assess one more parameter required by NaMaster, namely the beam or PSF of the instrument. The correct way to use the beam is to take the Fourier transform of the Gaussian PSF, i.e

$$PSF(x, \sigma) = \exp\left(\frac{-x(x+1)}{2\sigma^2}\right)$$

where σ is the resolution of the instrument in radians. Thus,

$$\sigma_{planck} = \frac{10\pi}{180} \text{ radians}$$

The fourier transform of the PSF is given by,

$$PSF'(l, \sigma) = \exp\left(\frac{-l(l+1)\sigma^2}{2}\right)$$

where l is the same multipole described above.

A test was performed to check the correct usage of beam which involved convoluting a test power spectrum using different techniques and testing out the beam on each of those convolved spectra to recover the original spectrum. Figure 14 shows the result of the test.

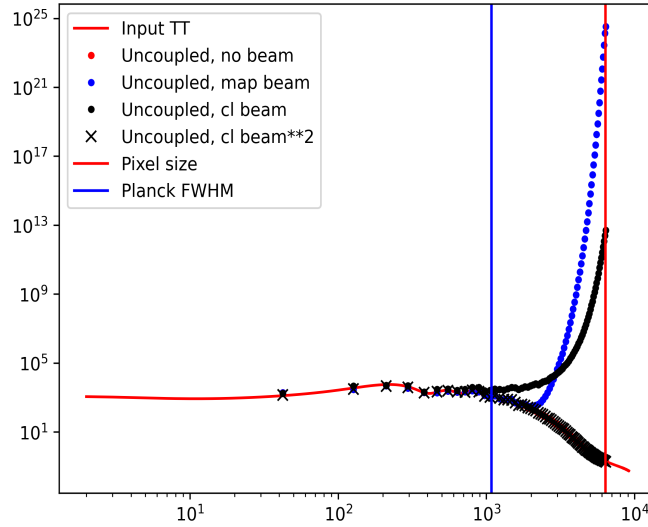


Figure 14: Beam usage using different simulations of convoluted spectra

3.5 Resulting Spectra

Finally, we have the pipeline set to churn out the power spectrum for any given map of the cluster. Note that the angular power spectra has to be first converted into its non-angular counterpart using the flat sky approximation, which has to be further converted to

its amplitude given by,

$$A_{\frac{\delta y}{y}} = \sqrt{\frac{k^2 P_{\frac{\delta y}{y}}(k)}{2\pi}}; \quad \frac{k}{2\pi} = \frac{1}{\lambda}$$

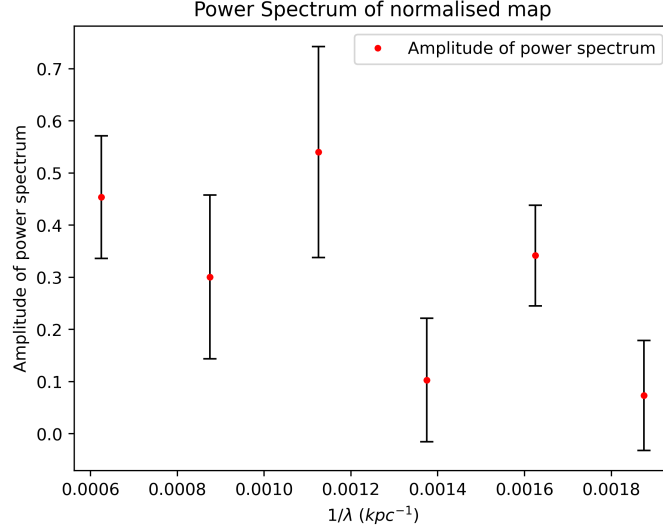


Figure 15: Amplitude of the auto-power spectrum of normalized y fluctuation map.

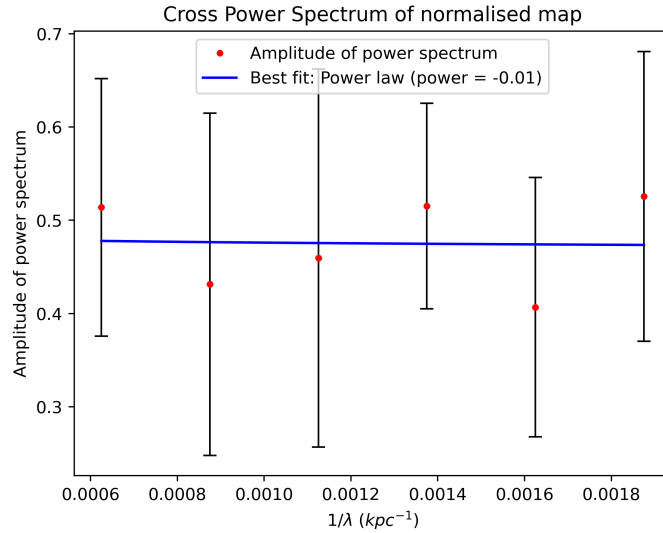


Figure 16: Amplitude of the cross-power spectrum of normalized y fluctuation map

We have carried out the analysis for both the original map which gave a relatively noisy auto-power spectrum, as well as used the cross-power spectra of half-ring y-maps so that the uncorrelated white noise is automatically cancelled. The power spectra of the normalized fluctuation maps have been plotted as shown in Figure 15 and 16.

We can clearly observe that the cross power spectrum appears to be much smoother with lower correlation between bins (Although it may appear otherwise due to different scales of the y-axes)

3.6 Checking parseval's theorem

Parseval's theorem can equip us with a useful test to check the validity of the computed power spectrum for any given map. For a 2D discrete Fourier transform, the theorem states that the variance of the original map should be equal to the integral of the power spectrum, i.e.

$$\frac{\sum_{n=1}^N (F(x, y) - F_{avg})^2}{N^2} = \int_{-\infty}^{\infty} P(f) df$$

where $F(x, y)$ is the original 2D map, N is the total number of discrete points in the map, f_{avg} is the mean, P is the power spectrum and f is the fourier frequency.

We proceeded to run another simulation of a map made up of sine waves (Figure 17) and found that the parseval's theorem checks out for fourier transforms using scipy and numpy modules. However, using the NaMaster package which computes the power spectrum, this led to some discrepancy. As of yet, we aren't sure about what's going wrong. A possible reason might be because NaMaster computes the estimated power spectrum in spherical harmonic space, by taking an average of power over all the $2l + 1$ "m" modes. However, further inspection is required before we can start using this theorem.

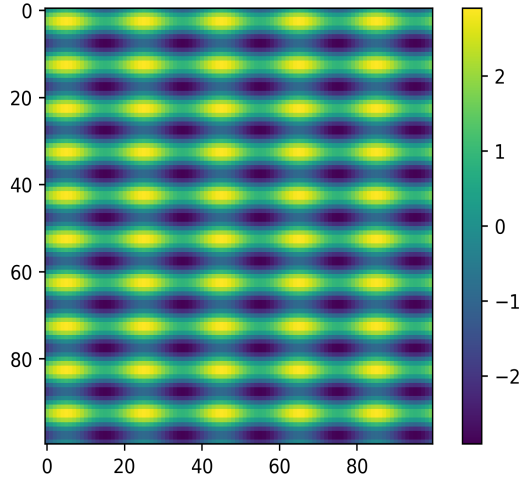


Figure 17: Simulated map used to check Parseval's theorem

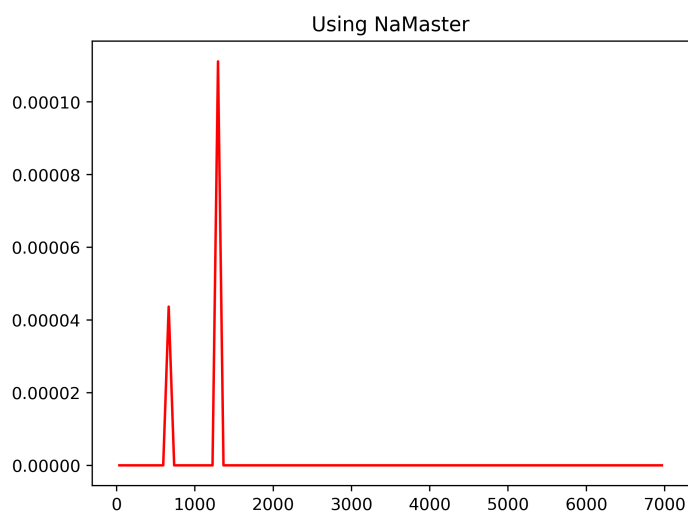


Figure 18: Angular Power spectrum C_l vs l using NaMaster

4 CHAPTER 4

PRESSURE PERTURBATIONS

Now that we have the pipeline in place to compute the power spectrum of both the y fluctuations and normalised y fluctuations map, the next step would be to convert it to a form which is physically interpretable, namely the pressure power spectrum. The relationship between the two is derived by introducing a new Window function $\tilde{W}(k_z)$. The entire procedure has been discussed in section 4.1 and boils down to,

$$P_y(k_\theta) = \int_{k_z} \frac{dk_z}{2\pi} \left| \tilde{W}(k_z, \theta) \right|^2 P_P(|k_\theta + k_z|)$$

Thus, we are already at a crossroads here cause because the pressure spectrum is stuck inside an integral of k_z . We are forced to make an assumption such that we can take it out of the integral, i.e. $k_z \ll k_\theta$. The validity of such an assumption has also been discussed in section 4.4. Under this assumption however, the relation reduces to

$$P_y(k_\theta) = P_P(|k_\theta|) \int_{k_z} \frac{dk_z}{2\pi} \left| \tilde{W}(k_z, \theta) \right|^2$$

Before computing these window function integrals, let us first look at what these are and where they come from.

4.1 Relation between y and Pressure power spectra

We start by calculating the correlation function in two different ways, and try relating them. For the SZ correlation between two points at θ and $\theta + r$, we have:

$$\begin{aligned} C(r) &= \left\langle \frac{\delta y}{\bar{y}}(\theta) \frac{\delta y}{\bar{y}}(\theta + r) \right\rangle \\ &= \int \frac{d^2 k_\theta}{(2\pi)^2} e^{ik_\theta r} P_y(k_\theta) \end{aligned}$$

where \bar{y} is the Fourier transform of $\frac{\delta y}{\bar{y}}$ and we have used:

$$\langle \bar{y}(k_\theta) \bar{y}(k'_\theta) \rangle = (2\pi)^2 P_y(k_\theta \delta_D^2)(k_\theta + k'_\theta)$$

where δ_D is the Dirac delta distribution.

We can also write y as integral over pressure along line of sight direction, taken along z -direction,

$$C(r) = \left\langle \frac{\delta y}{\bar{y}}(\theta) \frac{\delta y}{\bar{y}}(\theta + r) \right\rangle = \left\langle \frac{\int \bar{P}(\delta P \bar{P}) dz}{\int \bar{P} dz}(\theta) \frac{\int \bar{P}(\delta P / \bar{P}) dz}{\int \bar{P} dz}(\theta + r) \right\rangle$$

Now we define the window function as,

$$W(z, \theta) = \frac{\bar{P}}{\int \bar{P} dz} = \frac{m_e c^2}{\sigma_T} \frac{\bar{P}}{\bar{y}} = \frac{\bar{y}_{3D}}{\bar{y}_{2D}}$$

where $\bar{y}_{3D} = \frac{m_e c^2}{\sigma_T} \times \bar{P}$ and \bar{y}_{2D} is the just the usual y profile.

Assuming that it is independent of θ , we get:

$$\begin{aligned} C(r) &= \langle \int dz W \frac{\delta P}{\bar{P}}(\theta) \int dz' W \frac{\delta P}{\bar{P}}(\theta + r) \rangle \\ &= \int dz dz' \frac{d^3 k}{(2\pi)^3} \frac{d^3 k'}{(2\pi)^3} \frac{dk'_{z_1}}{2\pi} \frac{dk'_{z_2}}{2\pi} \tilde{W}(k_z - k'_{z_1}) \tilde{W}(k'_z - k'_{z_2}) \\ &\quad \times e^{i(k_\theta \dots \theta + k_z \dots z + k'_\theta \dots (\theta + r) + k'_z \dots z')} \langle \tilde{P}(k_\theta, k'_{z_1}) \tilde{P}(k'_\theta, k'_{z_2}) \rangle \end{aligned}$$

where we have defined \tilde{P} as the Fourier transfer of $\delta P / \bar{P}$ and \tilde{W} as the Fourier transform of W . Using

$$\langle \tilde{P}(k_\theta, k'_{z_1}) \tilde{P}(k'_\theta, k'_{z_2}) \rangle = (2\pi)^3 \delta_D^2(k_\theta + k'_\theta) \delta_D(k'_{z_1} + k'_{z_2}) P_P(|k_\theta + k_z|)$$

Using equation; we get the following relation between y and pressure power spectra as,

$$P_y(k_\theta) = \int \frac{dk_z}{2\pi} \left| \tilde{W}(k_z, \theta) \right|^2 P_P(|k_\theta + k_z|)$$

The same derivation has also been carried out by Khatri and Gaspari (2012).

Note: The Fourier convention adopted throughout the report is the following,

$$f(x) = \int \frac{d^n k}{(2\pi)^n} \tilde{f}(k) e^{ik \cdot x}$$

4.2 Computing the Window integrals

Equipped with the definition of Window function, we can now proceed to calculate

$$\int_{k_z} \frac{dk_z}{2\pi} \left| \tilde{W}(k_z, \theta) \right|^2 \equiv N(\theta)$$

Here, $\tilde{W}(k_z, \theta)$ is the partial fourier transform of $W(z, \theta)$ related by,

$$\tilde{W}(k_z, \theta) = \int_{-\infty}^{\infty} W(z, \theta) e^{-izk_z} dz$$

From section 4.1,

$$W(z, \theta) = \frac{m_e c^2}{\sigma_T} \frac{\bar{P}}{\bar{y}} = \frac{\bar{y}_{3D}}{\bar{y}_{2D}}$$

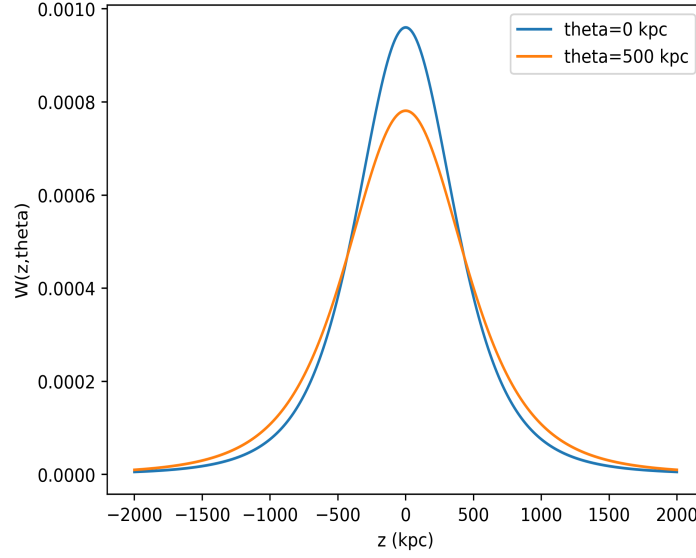


Figure 19: Window Function using the approximate beta model plotted for $\theta = 0, 500$ kpc.

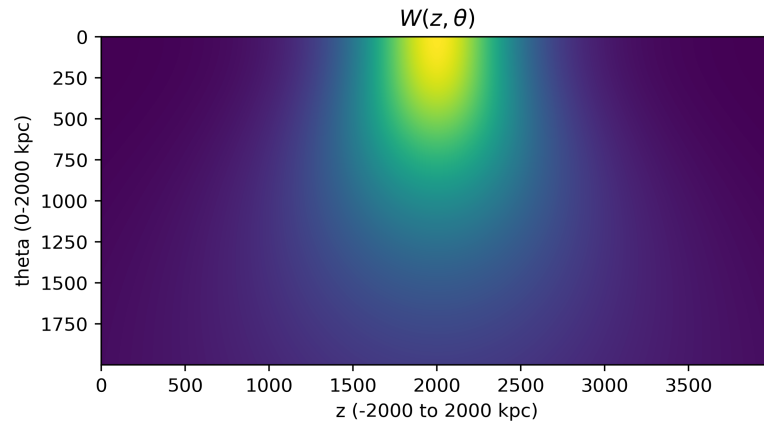


Figure 20: Heat map of $W(z, \theta)$ ranging over $0 < \theta < 2000$ kpc and $-2000 < z < 2000$ kpc

Using the beta model fit as an approximation for 3D and 2D y profiles,

$$W(z, \theta) = \frac{\bar{y}_{3D}}{\bar{y}_{2D}} = \frac{(y_0)_{3D}}{(1 + r^2/r_c^2)^{\beta_{3D}}} \times \frac{(1 + \theta^2/\theta_c^2)^\beta}{y_0}$$

with $r^2 = \theta^2 + z^2$. Using the values of $(y_0)_{3D}$, r_c , y_0 , θ_c , β , β_{3D} from Sections 2.2 and 2.3, the behaviour of this function was analyzed with respect to z and θ (Figures 19 and 20). Next, $\tilde{W}(k_z, \theta)$ was computed numerically (Figure 21) and integrated over all of k_z to obtain our final $N(\theta)$ (Figure 22).

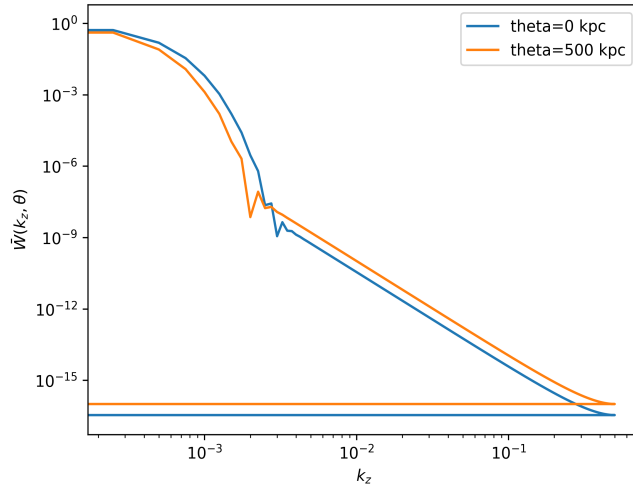


Figure 21: Partial Fourier transform of $W(z, \theta)$, i.e. $\tilde{W}(k_z, \theta)$ for $\theta = 0, 500$ kpc

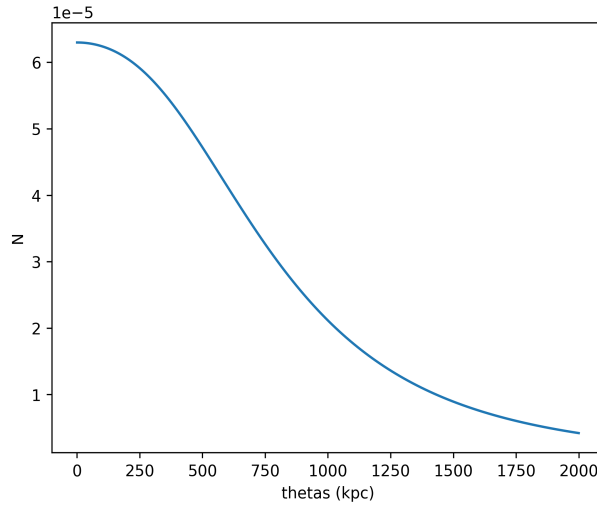


Figure 22: The final Window function integrals, i.e. $N(\theta)$ ranging over $0 < \theta < 2000$ kpc

Note: We observed that final $N(\theta)$ values were sensitive to the choice of our beta model parameters used in the Window function expression, namely the $(y_0)_{3D}$, r_c , y_0 , θ_c values. Surprisingly, it wasn't too sensitive to the choice of β and β_{3D} . Khatri and Gaspari (2012) had gotten slightly different values of these parameters. This may be due to the fact that they used the original y map as LIL instead of MILCA as well as the fact that they resorted to calculating the 3D y profile analytically using an Abel transform while we stuck to a numerical "onion peeling". However, the bottom line remains that neither of these methods have taken into account the PSF function while deprojecting. This leaves room for a lot of error in the values of $N(\theta)$ and subsequently the final pressure spectra. We may however take some solace in the fact that $N(\theta)$ turns out to be just a normalization factor in the end.

4.3 Pressure power Spectra

From the previous section ??, it is clear that the window function integrals (N 's) are a strong function of the physical distance θ . Thus, for a given y power spectrum, converting it to pressure won't be as straightforward. The relation between the two is now given by,

$$P_P(k_\theta) = \frac{P_y(k_\theta)}{N(\theta)}$$

and since we are working under the assumption that $k_z \ll k_\theta$, we can use $k \approx k_\theta$ where $k = \sqrt{k_\theta^2 + k_z^2}$ leaving us with,

$$P_P(k) = \frac{P_y(k)}{N(\theta)}$$

Keeping the θ dependence of N 's in mind, we decided to plot pressure spectra for different θ values. Figures 23 and 24 are the corresponding pressure spectra of the normalized y fluctuations spectra (Figures 15 and 16 *resp.*) Note that the amplitude in the 3D case is given by,

$$A_P = \sqrt{\frac{k^3 P_P(k)}{2\pi^2}} ; \quad \frac{k}{2\pi} = \frac{1}{\lambda}$$

Also note that the spectra for different θ 's only differ by a normalization, the shape of the curve remains the same. Again, we see that the pressure spectra corresponding to the cross spectrum of fluctuations appear to be smoother and less noisier than its auto spectrum counterpart.

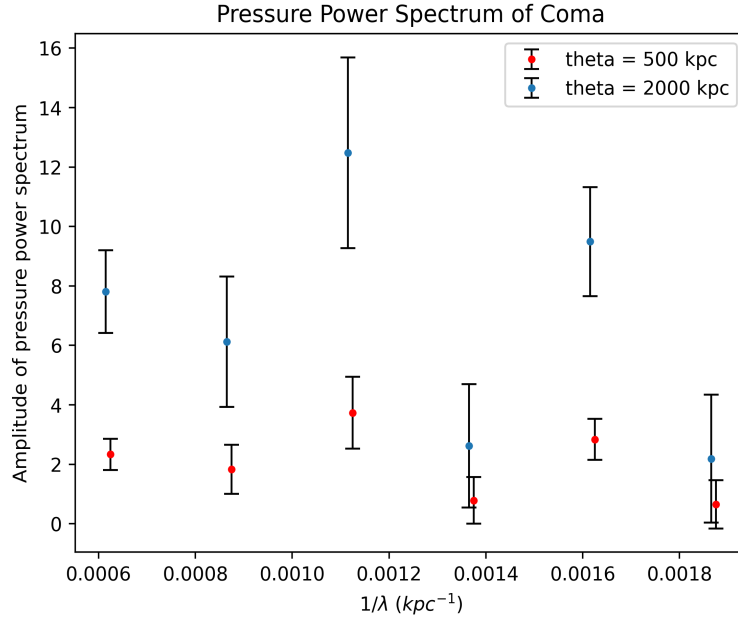


Figure 23: Amplitude of Pressure (auto) power spectra for $\theta = 500, 2000$ kpc

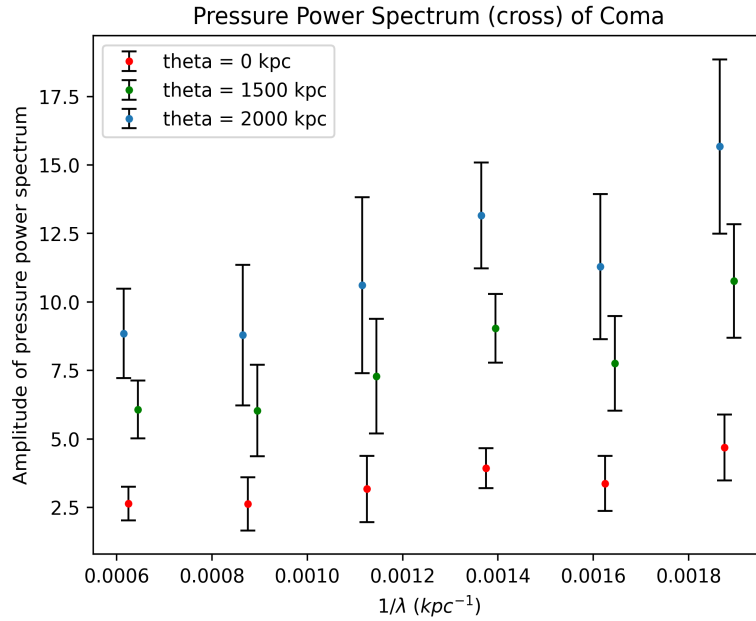


Figure 24: Amplitude of Pressure (cross) power spectra for $\theta = 500, 1500, 2000$ kpc

4.4 Validity of our assumptions

Now that we have computed the pressure spectra, we need to go back and check if any of our a priori assumptions have been violated in the process. Particularly, let us look at the assumption $k_z \ll k_\theta$ which was invoked to bring the pressure power spectrum out of the integral over k_z .

For our final pressure spectra (figures 23 and 24),

$$5 \times 10^{-4} < \frac{k}{2\pi} < 2 \times 10^{-3}$$

However, from figure 22 it is clear that for $\theta \lesssim 500$ kpc, the contribution of the $\frac{k_z}{2\pi} > 5 \times 10^{-4}$ part to the integral of the window function (i.e, the $N(\theta)$ values) cannot be neglected completely. This is in direct contradiction with our assumption since both k and k_z will take the same range of values violating $k_z \ll k_\theta$. The same issue also arises in Khatri and Gaspari (2012) and further inspection is required as of now.

5 ACKNOWLEDGEMENTS

We are extremely grateful for this opportunity to be working on this project with Dr. Yvette Perrott and Dr. Tulasi Nandan Parashar, Victoria University of Wellington. This project revealed to us the vast potential of Galaxy clusters and the intra-cluster medium, instilled wonderful insights about the astrophysics and cosmology of such large scale structures within our Universe.

We are thankful to our two supervisors, who provided us with proper guidance and direction, by making time, despite their busy schedules.

This project used data from European Space Agency's probe Planck, funded by ESA member states, NASA and Canada. We also had significant help from the NaMaster Package to calculate the power spectrum, developed by Prof. David Alonso, University of Oxford.

Thankfully,
Aditi and Chandraniva

6 BIBLIOGRAPHY

1. KHATRI, R., GASPARI, M.; Thermal SZ fluctuations in the ICM: probing turbulence and thermodynamics in Coma cluster with Planck, 2016
2. CROSTON, J. H., ARNAUD, M. AND POINTECOUTEAU, E., PRATT, G. W.; An improved deprojection and PSF-deconvolution technique for galaxy-cluster X-ray surface-brightness profiles, 2006
3. MCLAUGHLIN, DEAN E.; The Efficiency of Globular Cluster Formation, 1999
4. CHURAZOV, E., VIKHLININ, A., ZHURAVLEVA, I., SCHEKOCHIHIN, A., PARISH, I., SUNYAEV, R., FORMAN, W., BOHRINGER, H., AND RANDALL, S.; X-ray surface brightness and gas density fluctuations in the coma cluster, 2012
5. PYMASTER, by Dr. David Alonso - Python implementation of NaMaster Library documentation